Distributions of ionospheric irregularities measured by the C/NOFS satellite

Emanoel Costa CETUC/PUC-Rio, and Patrick A. Roddy Space Vehicles Directorate, AFRL, Kirtland AFB, NM, USA

Abstract

The Planar Langmuir Probe (PLP) onboard the C/NOFS satellite has been monitoring ionospheric plasma densities and their irregularities since May 2008. The PLP data and its processing which led to several detrended (unbiased) probability distributions of 1-s standard deviation of the measured irregularities will be described. These probability distributions will be presented and discussed for several combinations of geophysical parameters.

Introduction

The Communication/Navigation Outage Forecasting System (C/NOFS) satellite was launched on April 16, 2008 into a low inclination (13°), elliptical orbit (perigee and apogee approximately equal to 400 km and 850 km, respectively). Data from a suite of sensors on board the satellite drive an equatorial ionospheric model to forecast the onset of plasma instability, as well as its evolution into plasma bubbles. Due to its orbital period, these sensors are able to revisit neighbor regions in space at 90-min intervals, measuring different ionospheric parameters with high resolution. The list of C/NOFS science objectives has been organized into three categories: (1) to understand physical processes active in the background ionosphere and thermosphere in which plasma instabilities grow; (2) to identify mechanisms that trigger or quench the plasma irregularities; and (3) to determine how the plasma irregularities affect the propagation of electromagnetic waves. It is anticipated that, by the end of the C/NOFS mission, with the assimilation of data from other ground- and space-based instruments and systems (incoherent and coherent radars, SCINDA, DMSP, etc.), the understanding of the physics controlling the equatorial ionosphere will have advanced to the point that the operational objective will also be reached: to nowcast and forecast the formation of ionospheric irregularities and their effects on the propagation of electromagnetic waves to a high degree of accuracy. It should be observed that a 2-h to 6-h forecast is required, as well as an extended 72-h prediction (de La Beaujardière et al., 2004).

Interesting new observations which may be associated with the solar-minimum conditions that existed during the first months were reported very soon after the launch of the C/NOFS satellite. The detailed Introduction by Nishioka et al., 2011, summarized these finding, with direct links to the original references. Next, they discussed apparently contradictory observations of plasma density irregularities and VHF scintillation activity at Ancon, Peru, with the additional support of simultaneous data from a ground-based GPS network, a Digisonde, and the Jicamarca incoherent scatter radar. In continuation of the initial studies related with deep solar-minimum conditions, Huang et al., 2011, investigated the generation and evolution of plasma bubbles and broad plasma depletions based on three different evenings of C/NOFS observations. They proposed a new mechanism through which a series of plasma bubbles are created in the evening sector by the Rayleigh-Taylor instability. The longitudinal widths of the plasma bubbles continuously grow, in such a way that multiple bubbles with regular sizes can merge to form wide bubbles or a broad depletion. The plasma bubbles are quenched through their fillings with newly-produced particles generated by photoionization processes near dawn.

Additionally, results from electric field measurements by the C/NOFS vector electric field instrument (VEFI) were applied to the assimilative physics-based ionospheric model (PBMOD) (Su et al., 2009, Su et al., 2011) to reproduce post-midnight and dawn observations of large-scale density depletions in the Northern Hemisphere summer during solar-minimum conditions.

The above paragraphs illustrates the important role of one particular C/NOFS instrument, its onboard Planar Langmuir Probe (PLP), which has been monitoring ionospheric plasma densities and their irregularities with high resolution (at 512 Hz during satellite eclipses) almost seamlessly since May 2008. Considering that the end of the C/NOFS mission is on sight, it may be interesting to summarize some statistical results from the PLP measurements. This is the objective of the present contribution. Therefore, it complements previous work by Roddy et al., 2010, and Dao et al., 2011, which also analyzed data corresponding to low solar activity conditions. The first authors processed $\Delta N_i/N_i$ records, calculated from the standard deviation ΔN_i of ion density fluctuations around its 1-s average N_i, to provide statistics of the ability of the C/NOFS PLP to detect scintillation observed by the SCINDA network at Christmas Island (3°N, 157°W). The second authors defined the ambient density as an envelope $N_{i,env}$ connecting the local maxima of ion density measurements evaluated every 60 seconds (corresponding to approximately 450 km in space) with spline interpolation. Next, they subtracted the measurements from the envelope to obtain the deviation δN_i from the ambient density and computed the normalized density depletion $\delta N_i/N_{i,env}$. Finally, they

analyzed the average $\delta N_i/N_{i,env}$ in one-hour local time bins.

In the next section, the PLP data and its processing which led to several detrended (unbiased) probability distributions of 1-s standard deviation of the measured irregularities in the ion density ΔN_i will be described. Note that the parameter investigated by the present statistical studies is different from the ones analyzed by the references in the previous paragraphs. The reason for the present selection will also be provided in the next section. These probability distributions will be presented and discussed for several combinations of geophysical parameters (solar activity, altitude range, longitude sector, local time interval, season, and geomagnetic latitude interval). Conclusions from the analysis will be listed.

Data description and processing

PLP data is immediately available in individual daily files with 1-Hz resolution, but high-resolution data (512 Hz) is also available on request. Each 1-s record associates the Universal Time (s) to the corresponding average ion density N_i (cm^{-3}), standard deviation of the ion density ΔN_i (cm^{-3}), ratio $\Delta N_i/N_i$, as well as satellite latitude (degrees), longitude (degrees), and altitude (km). Figure 1 displays an example of PLP data acquired during a single orbit (between consecutive crossings of the geographic equator) centered on local solar midnight. Its top panel shows the measured one-second (green) and one-minute (black) average ion densities against the left vertical axis. This panel also shows the altitude of the satellite against the right axis (blue, with eclipse indicated by the heavily dotted line). The central panel shows spectrograms of the full 512 Hz data converted into units of distance with spectral power given in arbitrary units. The bottom panel represents the ground track of the satellite (red, heavily dotted during the eclipse) together with the magnetic equator (green).

The 1-s time series of the average ion density N_i allows different studies of irregularity structures with relatively large scale sizes. Indeed, considering the average C/NOFS satellite velocity and the well-known sampling theorem (Haykin, 1983), only structures with scale sizes greater than or equal to approximately 15 km are well characterized in the time series. On the other hand, each value of the standard deviation of the ion density ΔN_i indicates the strength of the small-scale scintillation-causing irregularities in the corresponding 1-s interval, associated with the integrated power in the spectrograms of Figure 1. According to Yeh and Liu, 1982, under the conditions leading to a parabolic approximation to the scalar wave equation, one has

$$-2ik\frac{\partial u}{\partial z}+\nabla_{\perp}^{2}u=-k^{2}(\delta\varepsilon)u= 4\pi r_e(\delta N)u=4\pi r_e\Delta N_i(\delta\eta)u \quad (1)$$

In equation (1), u is the complex amplitude of the transionospheric signal, k is the free-space wavenumber, z is aligned with the propagation direction, $\nabla_{\perp}^{2}$ is the transverse component of the Laplacian operator, $\delta\varepsilon$ and δN are the zero-mean random permittivity and electron density fluctuations of the medium, and $r_e = 2.818 \times 10^{-15}$ m is the classical electron radius. Note that δN has been recast in the form $\Delta N_i(\delta\eta)$, where $\delta\eta$ is the normalized (zero-mean and unit-standard deviation) electron density fluctuations of the medium, which highlights the fundamental role of the absolute values of the standard deviation of the ion density ΔN_i in the development of scintillation of transionospheric signals, explaining the selection of this parameter for the present study. Indeed, as stressed by Yeh and Liu, 1982, the above is the basic equation upon which ionospheric scintillation theories are developed.

PLP data from two different years (01 October 2008 to 30 September 2009 and 01January 2012 to 31 December 2012) are selected for analysis. The first data set corresponds to solar minimum conditions and the second is as close to solar maximum conditions of solar cycle 24 as possible at the time of the analysis.

The results from the analysis show how the standard deviation of the ion density ΔN_i (cm^{-3}) which are greater than specified thresholds ($\Delta N_i > \Delta N_{ith}$) are statistically distributed, as functions of several combinations of the following parameters: (i) solar activity; (ii) altitude range; (iii) longitude sector; (iv) local time interval; (v) season; and (vi) geomagnetic latitude interval. The effects from the solar activity are represented by the differences between the results from the two selected years. Four local-time intervals {[18 LT, 21 LT); [21 LT, 24 LT); [00 LT, 03 LT); [03 LT, 06 LT)} and four seasons (days 34 to 125 for the March equinox, 126 to 216 for the June solstice, 217 to 307 for the September equinox and 308 to 33 for the December solstice) are considered.

To study the altitude distribution of $\Delta N_i > \Delta N_{ith}$, four equal-size ranges are assumed: [400 km, 500 km); [500 km, 600 km); [600 km, 700 km); and [700 km, 800 km). Samples of ΔN_i corresponding to satellite positions outside these intervals are discarded. This selection of altitude intervals, in addition to keeping uniformity, also takes into account the fact that, with age, the C/NOFS satellite no longer reaches the initial apogee (850 km), as observed in Figure 1.

On the other hand, five uneven longitude sectors are selected: South-American [280°-330°), African [330°-060°), Indian [060°-090°), Asian [090°-140°), and Pacific [140°-280°). As indicated in Figure 1, the magnetic declination remains relatively constant in each of these sectors. In fact, this is also true throughout the three central sectors, where the geographic and magnetic equators are approximately parallel to each other. They are separated to facilitate possible comparisons between the present results and those from independent studies performed in the three sectors. The definition of the above longitude sectors also permits the observation of seasonal and longitudinal occurrence patterns of equatorial irregularities according to the alignment between the dusk terminator and the geomagnetic flux tubes (Abdu et al., 1981b, Tsunoda, 1985).

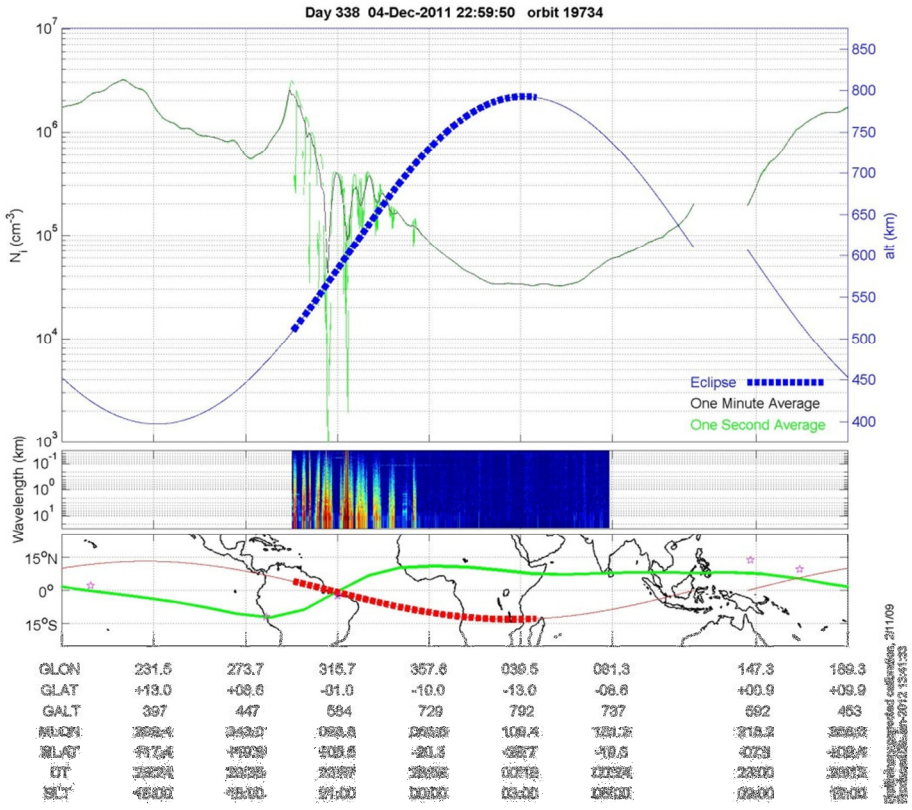

Figure 1: Orbit 19734, 04 December 2011. (top) One-minute average ionospheric density (black line); one-second average density (green line); and satellite altitude (blue line). (middle) FFT from the 512 Hz PLP data. (bottom) Map with satellite trajectory (red) and magnetic equator (green). Thick dotted lines indicate when the C/NOFS satellite is in darkness.

The magnetic latitude ψis approximately determined from the relationship tan ψ = (1/2) tan *I*, where the magnetic inclination *I* is obtained from version 11 of the International Geomagnetic Reference Field model (IGRF-11) (International Association of Geomagnetism and Aeronomy, Working Group V-MOD, 2010) for the corresponding C/NOFS satellite position. To study the magnetic latitude distribution of $\Delta N_i > \Delta N_{ith}$, three equal-size intervals are considered: [-20°, -10°], [-5°, 5°], and [10°, 20°]. Irregularities outside these intervals are not considered by magnetic latitude studies. The second interval is centered at the magnetic equator and the other two should ordinarily include the peaks of the equatorial anomaly. It should be observed that, due to the structure of the geomagnetic field and its orbital characteristics, the C/NOFS satellite never transits through the third magnetic latitude interval [10°, 20°] of the African, Indian and Asian longitude sectors, as also inferred from Figure 1.

As expected, the local time of the C/NOFS satellite is evenly distributed between the four selected intervals {[18 LT, 21 LT); [21 LT, 24 LT); [00 LT, 03 LT); [03 LT, 06 LT)}, for evening hours. Uniformity also holds with regard to the seasonal distribution.

On the other hand, it is evident that relative frequencies of observables in the longitude sectors are affected by their different widths.

Additionally, it should be observed that, also due to its orbital characteristics, the C/NOFS satellite is not neutral with respect to altitude and latitude measurements. Indeed, Figure 2 shows the probability density functions (pdf) of the C/NOFS satellite altitude and geographic latitude, resulting from the data files and predicted by a theoretical model (Fortes et al., 1999). Each of the curves in Figure 2 is normalized in such a way that the pdfs values at their break points add to one.

The top plot clearly shows the good agreement between the predicted and the initial altitude pdfs corresponding to the year 2008, as well as the progressive departure from them over the years. On the other hand, the good agreement between the predicted and the geographic latitude pdfs persisted throughout the years. It is also important to note that, as previously mentioned, the C/NOFS satellite transits through the selected altitude and geographic longitude intervals with different probabilities. For example: (1) the probability for the lower altitude interval [400 km, 500 km) is greater than that for the one immediately above [500 km, 600 km); and (2) the probability for the geographic latitude interval [-13°, 8°) is greater than that for any other interval of the same length. From the lower panel of Figure 1, one can easily conclude

that the absence of uniformity in the distribution of the geographic latitude of the C/NOFS satellite also assigns different probabilities to its presence in the selected magnetic latitude intervals.

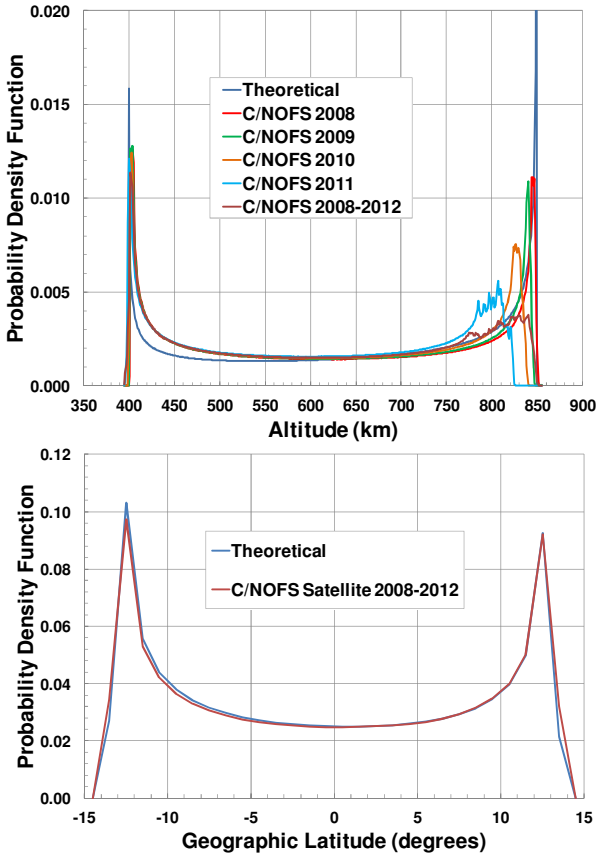

Figure 2: Probability density functions (pdfs) of the C/NOFS satellite altitude (top) for different years and an extended period, as well as of the geographic latitude (bottom) for the same extended period, estimated from the data files. Also shown are the corresponding pdfs predicted by a theoretical model (Fortes et al., 1999) assuming nominal orbital parameters (inclination 13°, perigee and apogee approximately equal to 400 km and 850 km, respectively). Each of the above curves is normalized in such a way that the pdfs values at their break points add to one.

Considering the above observations, the detrended (unbiased) probability distribution of $\Delta N_i > \Delta N_{ith}$ between each of different combinations of parameter intervals is obtained as follow. Initially, the probabilistic distributions of: (i) the occurrence of the C/NOFS satellite; and (ii) the biased ocurrence$\Delta N_i > \Delta N_{ith}$ within each of different combinations of parameter classes is separately determined. Next, each individual value of the latter is divided by the corresponding value of the former. Note that probabilities of certain occurrences of the C/NOFS satellite are equal to zero, as indicated by the last sentence of the previous paragraph specifying magnetic latitude intervals. However, the corresponding probabilities of $\Delta N_i > \Delta N_{ith}$ are also necessarily equal to zero and the above divisions are avoided in these cases.

Finally, the set of resulting values are renormalized in such a way that their final sum represents the global probability of $\Delta N_i > \Delta N_{ith}$ being exceeded. As illustrations of the application of the above procedures, the detrended probability distributions of $\Delta N_i > \Delta N_{ith}$ have been independently determined for the: (i) altitude ranges, local time interval and longitude sectors (total of 4 x 4 x 5 = 80 classes); and (ii) altitude ranges, magnetic latitude intervals and longitude sectors (total of 4 x 3 x 5 = 60 classes).

Results

Totals of 11,085,676 and 12,990,898 samples of ΔN_i resulted from the C/NOFS PLP measurements during the evening hours (between 18 h LT and 06 h LT) of the respective years 2008-2009 and 2012 in the altitude interval [400 km, 800 km). The observed absolute maximum value of ΔN_i corresponded to a negligibly low probability. For the current purposes, the maximum value of ΔN_i also exceeded with a significant probability was taken as 3.2×10^5 cm^{-3} [$\log(\Delta N_i) = 5.5$]. Considering this significant maximum value, the threshold levels $\log(\Delta N_i) > 3.5$ and $\log(\Delta N_i) > 4.5$ were adopted. It should be stressed that the global percentages of the above samples that exceeded the threshold $\log(\Delta N_i) > 3.5$ were approximately 0.37 % and 7.78 % for the years 2008-2009 and 2012, respectively, and that exceeding the threshold $\log(\Delta N_i) > 4.5$ was approximately 0.33 % for the year 2012. The highest threshold level was exceeded during the solar-minimum year 2008-2009 with such a low probability that the corresponding distributions will not be shown.

The next Figures show detrended probability distributions of ΔN_i in a fixed format for: (a) 2008-2009 and $\log(\Delta N_i) > 3.5$; (b) 2012 and $\log(\Delta N_i) > 3.5$; (c) 2012 and $\log(\Delta N_i) > 4.5$. The difference between the vertical scales of the two panels (a) and (c) and that of panel (b), by a factor of ten, should be observed.

Figure 3 displays the detrended probability distributions of ΔN_i as functions of altitude ranges and longitude sectors. For reference, the greatest detrended probabilities of panels (a) and (c) are approximately equal to that for the African sector in the [600 km, 700 km) altitude range of panel (b).

For the year 2008-2009, irregularities with $\log(\Delta N_i) > 3.5$ are very rare above 600 km, for all longitude sectors. The probabilities decrease very fast with the altitude range for each longitude sector. For both altitude ranges [400 km, 500 km) and [500 km, 600 km), the probabilities are distinctly larger in the American sector. In sequence, they decrease in the following order of the longitude sectors: Pacific, African, Asian, and Indian.

For the year 2012, the probabilities of irregularities with $\log(\Delta N_i) > 3.5$ decreased by a factor greater than two between altitude ranges for each longitude range, reaching the highest altitude range [700 km, 800 km) with relatively small but non negligible probabilities. This is particularly true in the American and the African sectors.

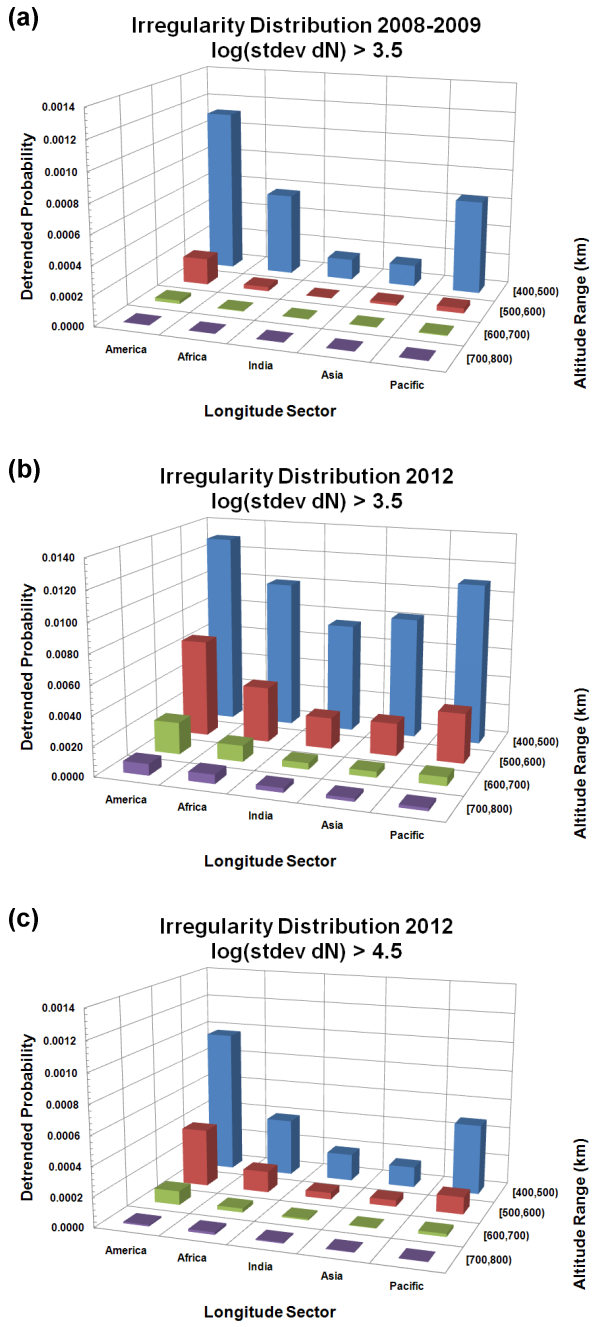

Figure 3: Detrended probability distributions of ΔN_i as functions of altitude ranges and longitude sectors for: (a) 2008-2009 and $\log(\Delta N_i) > 3.5$; (b) 2012 and $\log(\Delta N_i) > 3.5$; (c) 2012 and $\log(\Delta N_i) > 4.5$, which add to 0.37 %, 7.87 %, and 0.33 %, respectively.

The same dependence of the probabilities with the longitude sector described previously (American, Pacific, African, Asian, and Indian) is observed for the lowest altitude range. However, the probabilities associated with the African and Pacific sectors are approximately equal for the altitude range [500 km, 600 km) and the former are larger than the latter for the two highest altitude ranges.

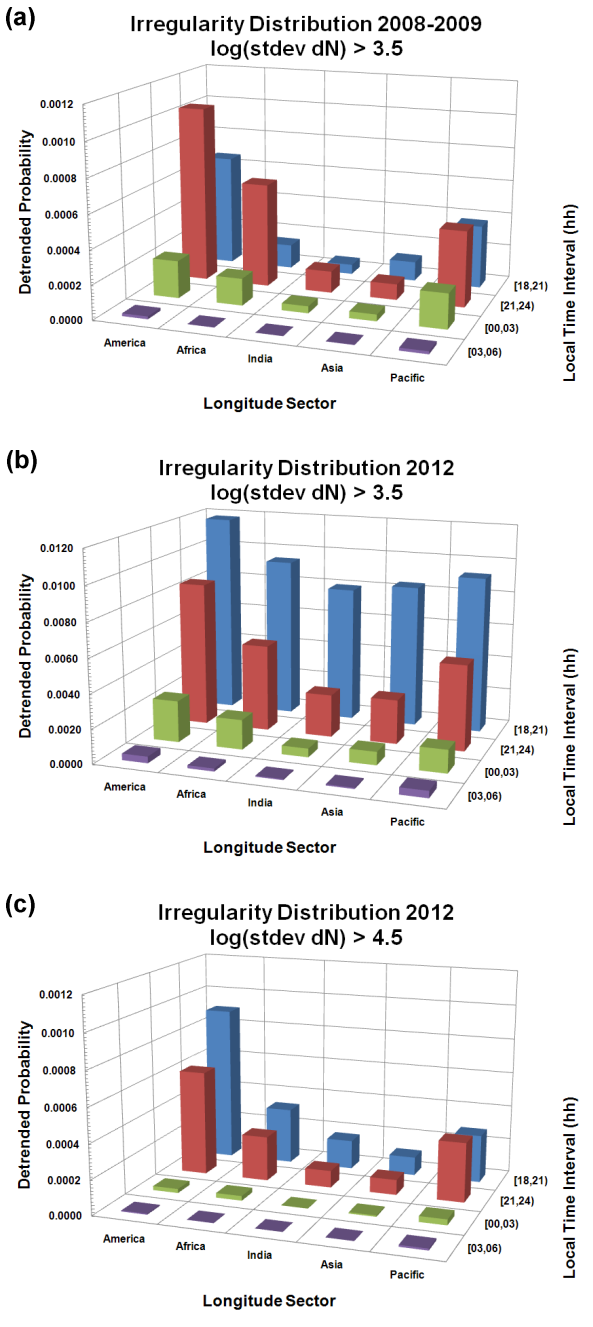

Figure 4: Detrended probability distributions of ΔN_i as functions of local time intervals and longitude sectors for: (a) 2008-2009 and $\log(\Delta N_i) > 3.5$; (b) 2012 and $\log(\Delta N_i) > 3.5$; (c) 2012 and $\log(\Delta N_i) > 4.5$, which add to 0.37 %, 7.87 %, and 0.33 %, respectively.

The irregularities with $\log(\Delta N_i) > 4.5$ for the year 2012 virtually do not reach the highest altitude range [700 km, 800 km). Additionally, the probability associated with the African sector is greater than that for the Indian sector for the altitude range [400 km, 500 km). Except for these observations and for the difference between their vertical scales by a factor of ten, the distributions of probabilities displayed in panels (b) and (c) of Figure 3 are similar.

Figure 4 displays the detrended probability distributions of ΔN_i as functions of local times and longitude sectors. For reference, the greatest detrended probabilities of panels (a) and (c) are slightly smaller than that for the Pacific sector and the [00 LT, 03 LT) local time interval of panel (b).

For the year 2008-2009, irregularities with $\log(\Delta N_i) > 3.5$ are extremely rare after 03 LT, for all longitude sectors. For each longitude sector but the Asian, the probabilities peak in the [21 LT, 24 LT) local time interval, being lower in the local time interval [18 LT, 21 LT) by factors varying from 1.2 to 4.3. Additionally, they are substantially lower than their corresponding peak values in the later local time interval [00 LT, 03 LT), by factors varying from 2.2 to 4.7.

On the other hand, the probabilities of irregularities with $\log(\Delta N_i) > 3.5$ for the year 2012 peak in the [21 LT, 24 LT) local time interval for all longitude sectors. These probabilities are very small but non negligible even in the local time interval [03 LT, 06 LT), particularly for the American, Pacific and African longitude sectors. Also, the probabilities decrease with the local time intervals, by factors ranging from 1.4 to 3.2 within the intervals [18 LT, 21 LT) and [21 LT, 24 LT) and 3.0 to 5.0 within the intervals [21 LT, 24 LT) and [00 LT, 03 LT).

The irregularities with $\log(\Delta N_i) > 4.5$ for the year 2012 also peak in the [21 LT, 24 LT) local time interval for all longitude sectors but the Pacific, and are virtually nonexistent after 24 LT. With the noted exception, the probabilities decrease between the intervals [18 LT, 21 LT) and [21 LT, 24 LT) by factors ranging from 1.2 to 1.5.

Conclusions

Statistical analysis of C/NOFS PLP data show uneven probability distributions of ΔN_i, as functions of several combinations of the following parameters: (i) solar activity; (ii) altitude range; (iii) longitude sector; (iv) local time interval.

Some patterns have been identified for these distributions. In particular, their probabilities increase with the solar activity and decrease in the following order of the longitude sectors: (i) American, (ii) Pacific and African, and (iii) Asian, and Indian.

References

Abdu, M. A., J. A. Bittencourt, I. S. Batista, 1981, Magnetic declination control of the equatorial F region dynamo electric field development and Spread F: Journal of Geophysical Research, 86, 11,443-11,446.

Dao, E., M. C. Kelley, P. Roddy, J. Retterer, J. O. Ballenthin, O. de La Beaujardiere, and Y.-J. Su, 2011, Longitudinal and seasonal dependence of nighttime equatorial plasma density irregularities during solar minimum detected on the C/NOFS satellite: Geophysical Research Letters, 38, L10104/01- L10104/07.

de La Beaujardière, O., and the C/NOFS Science Definition Team, 2004, C/NOFS: a mission to forecast scintillation: Journal of Atmospheric Solar Terrestrial Physics, 66, 1573-1591.

Fortes, J. M. P., R. Sampaio-Neto, J. E. A. Maldonado, 1999, An analytical method for assessing interference in interference environments involving NGSO satellite networks: International Journal of Satellite Communications and Networking, 17, 399–419.

Haykin, S., 1983, Communication Systems: John Wiley and Sons, Inc.

Huang, C.-S., O. de La Beaujardiere, P. A. Roddy, D. E. Hunton, R. F. Pfaff, C. E. Valladares, and J. O. Ballenthin, 2011, Evolution of equatorial ionospheric plasma bubbles and formation of broad plasma depletions measured by the C/NOFS satellite during deep solar minimum: Journal of Geophysical Research, 116, A03309/01- A03309/11.

International Association of Geomagnetism and Aeronomy, Working Group V-MOD. Participating members, Finlay, C. C., et al., 2010, International Geomagnetic Reference Field: the eleventh generation: Geophysical Journal International, 183, 1216–1230.

Nishioka, M., Su. Basu, S. Basu, C. E. Valladares, R. E. Sheehan, P. A. Roddy, and K. M. Groves, 2011, C/NOFS satellite observations of equatorial ionospheric plasma structures supported by multiple ground-based diagnostics in October 2008: Journal of Geophysical Research, 116, A10323/01- A10323/12.

Roddy, P. A., D. E. Hunton, J. O. Ballenthin, K. M. Groves, 2010, Correlation of in situ measurements of plasma irregularities with ground-based scintillation observations: Journal of Geophysical Research, 115, A06303/01-A06303/06.

Su, Y.-J., J. M. Retterer, O. de La Beaujardiere, W. J. Burke, P. A. Roddy, R. F. Pfaff Jr., G. R. Wilson, and D. E. Hunton, 2009, Assimilative modeling of equatorial plasma depletions observed by C/NOFS: Geophysical Research Letters, 36, L00C02/01- L00C02/04.

Su, Y.-J., J. M. Retterer, R. F. Pfaff, P. A. Roddy, O. de La Beaujardière, and J. O. Ballenthin, 2011, Assimilative modeling of observed postmidnight equatorial plasma depletions in June 2008: Journal of Geophysical Research, 116, A09318/01- A09318/11.

Tsunoda, R. T., 1985, Control of the seasonal and longitudinal occurrence of equatorial scintillations by the longitudinal gradient in integrated E region Pedersen conductivity: Journal of Geophysical Research, 90, 447-456.

Acknowledgments

Emanoel Costa has been supported by AFOSR Award no. FA9550-12-1-0031 during this ongoing work.